metals

MDPI

Article

Biocompatibility, Corrosion Resistance, and Wear Resistance of TiNbZr-Based Composites Reinforced with Borides

Maxim Ozerov [1,*], Vitaly Sokolovsky [1,*], Marina Gazizova [1], Elizaveta Povolyaeva [1,2], Damir Tagirov [1], Maxim Yapryntsev [1], Firuz Yunusov [3] and Sergey Nadezhdin [1]

[1] Laboratory of Bulk Nanostructured Materials, Belgorod State University, Belgorod 308015, Russia; smolyakovamarina@bsu.edu.ru (M.G.); povolyaeva@bsu.edu.ru (E.P.); tagirov@bsu.edu.ru (D.T.); yaprintsev@bsu.edu.ru (M.Y.); nadezhdin@bsu.edu.ru (S.N.)
[2] World-Class Research Center "Advanced Digital Technologies", State Marine Technical University, Saint Petersburg 198095, Russia
[3] State Marine Technical University, Saint Petersburg 198095, Russia; yunusov.firuz@mail.ru
* Correspondence: ozerov@bsu.edu.ru (M.O.); sokolovskiy@bsu.edu.ru (V.S.); Tel.: +7-4722-58-54-16 (M.O. & V.S.)

Abstract: TiNbZr-(Ti,Nb)B composites were produced by vacuum arc melting; the weights of TiB_2 in the charge mixture were 0.7 wt. % (Alloy A) and 4.0 wt. % (Alloy B). In addition, unreinforced TiNbZr alloy specimens were fabricated without the addition of TiB_2. The microstructure of the TiNbZr-(Ti,Nb)B composites consisted of the TiNbZr β matrix and (Ti,Nb)B fibers. The (Ti,Nb)B fibers had a needle-like shape with an average diameter of ~0.4 and ~2.0 μm for Alloys A and B, respectively. The volume fraction of borides was found to be ~2.5 and ~12.4% for Alloys A and B, respectively. The presence of 12.4 vol.% of (Ti,Nb)B reduced the corrosion resistance of Alloy B in comparison with that of the TiNbZr alloy and Alloy A, which showed rather similar values of corrosion resistance. It was found that the addition of the TiB_2 to the TiNbZr alloy led to a decrease in the friction coefficient; when adding 0.7% TiB_2 to the alloy (Alloy A), the friction coefficient decreased from 1.15 to 1.13, and when the percentage of TiB_2 in the alloy increased to 4% (Alloy B), the friction coefficient decreased by ~2 times from 1.15 to 0.58. The full biocompatibility of TiNbZr-(Ti,Nb)B composites was demonstrated; no significant differences from the unreinforced state and alloy were found.

Keywords: medium-entropy alloy; metal–matrix composite; boride fibers; corrosion resistance; tribological properties; microstructure; biocompatibility

check for updates

Academic Editor: Damien Fabrègue

Received: 25 November 2024
Revised: 30 January 2025
Accepted: 4 February 2025
Published: 25 February 2025

Citation: Ozerov, M.; Sokolovsky, V.; Gazizova, M.; Povolyaeva, E.; Tagirov, D.; Yapryntsev, M.; Yunusov, F.; Nadezhdin, S. Biocompatibility, Corrosion Resistance, and Wear Resistance of TiNbZr-Based Composites Reinforced with Borides. *Metals* **2025**, *15*, 240. https://doi.org/10.3390/met15030240

Copyright: © 2025 by the authors. Licensee MDPI, Basel, Switzerland. This article is an open access article distributed under the terms and conditions of the Creative Commons Attribution (CC BY) license (https://creativecommons.org/licenses/by/4.0/).

1. Introduction

Today, titanium alloys, in particular the Ti-6Al-4V alloy, are attracting more and more claims against their use as implants in the human body [1]. For example, insufficiently high strength characteristics and hardness indicators, as well as low resistance to the contact wear of titanium and its alloys, can significantly limit their industrial application. It should also be noted that the possibilities of alloying biomedical titanium alloys are significantly limited due to the limited number of chemical elements that are harmless to the human body [1]. For example, the aviation Ti-6Al-4V alloy, which is widely used in medicine, contains vanadium, which is toxic to humans [2], and aluminum, which can cause neurological and genotoxic side effects on the human body [3,4]. It has been shown by previous studies that it is possible to increase the strength of titanium alloys without harming their biocompatibility by alloying them with elements that are harmless to the human body, such as Mo, Zr, Nb,

etc. [5,6], many of which are beta (body-centered cubic; bcc)-stabilizers. Many recent studies have shown that the medium-entropy equiatomic alloy Ti–Nb–Zr, with a chemical composition that includes some of the most bioinert elements, is incredibly promising for use in orthopedics as implants due to its high balance of strength and ductility [5,7]. Another very important characteristic of orthopedic implants is associated with their elastic modulus [8], since a large difference between the Young's modulus of the implant material and that of the bone can cause a so-called "shielding" effect, leading to repeated surgical intervention [9,10]. Currently, it is known that alloys of the Ti–Nb–Zr system show much lower values of Young's modulus, equal to 48–64 GPa, compared to the Ti-6Al-4V alloy (Young's modulus: 110 GPa), alloys based on the Co–Cr system (Young's modulus: 210–232 GPa) and 316L stainless steel (Young's modulus: 200 GPa), and are already close to the values of Young's modulus of bone tissue (~27 GPa) [11,12]. It is also necessary to note the beneficial effect of Zr, which suppresses surface phosphates, negatively affecting the interaction of bone tissues with the implant [13]. It is worth noting that previous studies confirmed the good biocompatibility of Ti–Nb–Zr alloys [14,15]. Thus, it can be said that the Ti–Nb–Zr system alloys are some of the best candidates for the development and implementation into the production of absolutely safe biomedical alloys with a high range of competitive advantages.

Meanwhile, applications of medium-entropy alloys of the Ti–Nb–Zr system can be limited due to their relatively low strength, hardness, and wear resistance [1,5,7]. One of the most effective ways to increase the strength of titanium-based alloys is using TiB particles (fibers) as a reinforcing component. A similar approach has been adopted for enhancing the strength and hardness of titanium and its alloys [16–18], since TiB fibers have (i) a good crystallographic relationship with the titanium matrix, (ii) a similar coefficient of thermal expansion with Ti, and (iii) good thermal stability [19–21]. The few studies describing the strengthening of Ti–Nb–Zr alloys using borides show rather optimistic results [22,23]. The addition of TiB particles to the Ti–35Nb–5.7Ta–7.2Zr (at.%) alloy resulted in a significant increase in strength with a slight increase in the Young's modulus of the resulting composite, but it also reduced its plasticity [24]. It should be noted that our recent works [25–27] also showed a positive effect of boride reinforcements on the strength properties of the equiatomic TiNbZr alloy without any negative impact on the cytotoxicity and Young's modulus.

Despite the extensive work focusing on some mechanical properties of Ti (Ti-alloys, Ti-rich alloys)–TiB composites, their biocompatibility, corrosion, and wear resistance have been studied to a significantly less extent. The excellent biocompatibility of the Ti–TiBw composites was reported in [28]; the obtained results suggest that fibroblasts attach, proliferate, and achieve confluence when in contact with the Ti–TiBw composites, exhibiting normal morphology. Furthermore, the cells show a favorable growth rate when cultured with the composite for 48 h. The Ti–TiBw composite demonstrated excellent blood biocompatibility with a low hemolysis level (0.12%) in comparison with CP Ti (0.17%) and Ti-6Al-4V (0.36%) [28]. It is also impossible not to mention the well-known positive effect of boron on the human body [29,30]. The existing studies on the corrosion properties and wear resistance of Ti (Ti-alloys, Ti-rich alloys)–TiB composites generally show the absence of a negative effect from the presence of borides in the titanium matrix [31–38]. In the works of [39,40], it was shown that boride-based coatings do not lead to a critical decrease in the corrosion resistance of CP titanium and the Ti-6Al-4V alloy. At the same time, the effect of TiB particles on the corrosion resistance and wear resistance of the equiatomic Ti–Nb–Zr matrix, as well as its biocompatible properties, remains almost unexplored. In a few works [41–43], the effects of boron alloying on the biocompatibility, wear resistance, and corrosion properties of the Ti–13Zr–13Nb alloy were investigated, but no positive

effect was obtained. Thus, the corrosion resistance, wear resistance, and biocompatibility of composites based on the equiatomic TiNbZr alloy with different contents of borides were studied in the present work.

2. Materials and Methods

The laboratory versions of the composite ingots (~50 g) were obtained by vacuum arc melting in a high-purity argon environment at an operating temperature of 3500 °C for 60 min, for which metal granules of Ti, Nb and Zr (purity $\geq$ 99.9 wt. % in each case) were used with two weight variations of TiB_2 powder (purity 99.9%). The weight fractions of the TiB_2 powder were 0.7 and 4.0 wt. % (hereinafter, the corresponding states are denoted as Alloy A and Alloy B, respectively). The ratio between the Ti, Nb and Zr elements was 1:1:1 (i.e., the equiatomic proportion). The unreinforced TiNbZr alloy was also fabricated using the same method without adding TiB_2. The residual porosity measured by hydrostatic weighing using a Porotech 3.1 automated standard porosimeter (Porotech Ltd., Toronto, Canada) and by metallographic analysis was $\leq$ 0.5%. Table 1 shows the chemical compositions of the resulting alloys.

Table 1. The atomic percent of each element in the studied alloys.

Alloy	Element	At.%
Alloy A	Ti	33.47
	Nb	32.56
	Zr	32.44
	B	1.53
Alloy B	Ti	32.71
	Nb	29.03
	Zr	29.15
	B	9.11

The initial microstructure of the as-cast composites was studied by scanning electron microscopy (SEM). Specimens were prepared for SEM examination by stepwise careful mechanical polishing. Microstructure imaging was performed on the perfectly polished surfaces of the samples. An FEI Quanta 600 FEG microscope (Thermo Fisher Scientific, Hillsboro, OR, USA) operating at 30 kV was used for the SEM studies. The linear intercept method was employed to quantify the average lengths and diameter of boride fibers. The Digimizer software version 4.3.0 (MedCalc Software Ltd., Ostend, Belgium) was used for calculations under this method.

Corrosion resistance was determined electrochemically using a P-20X8 multichannel potentiostat/galvanostat (Elins, Moscow, Russia) and a standard three-electrode cell consisting of a carbon counter electrode, the sample used as a working electrode, and an Ag/AgCl electrode used as a reference electrode connected to a Luggin capillary bridge. The tests were performed in Ringer's solution (0.9% NaCl solution, pH 7.8) at room temperature. The tested area of each specimen was $\geq$1.0 cm^2. The measurements were conducted for 90 min using the open circuit potential (OCP). The potentiodynamic polarization curves were then measured from $-$500 mV to 5000 mV at a scanning rate of 2 mV/s. After the tests, all the specimens were washed in distilled water and air-dried.

The wear resistance study was carried out using a CSM Instruments high-temperature tribometer (CSM Instruments, Peseux, Switzerland) under dry friction in air at room temperature using the ball-on-disk test scheme. The selected test type complies with the ASTMG99-959 [44] and DIN50324 [45] international standards. A 6 mm-diameter ball made of 100Cr6 steel was used as a counterbody. The load on the counterbody was 0.25 N. The

friction velocity was 10 cm/s. Counterbody wear was estimated by measuring the wear scar diameter and then calculating the wear factor. The wear resistance of the samples was estimated according to the volume of entrained material, which was calculated based on the cross-sectional area of the wear track obtained using a Sutronic 25 contact profilometer (Taylor Hobson Ltd., Leicester, Great Britain). Furthermore, the wear track morphology was studied using an FEI Quanta 600 FEG scanning electron microscope to identify the destruction features and determine the wear mechanisms.

Erosive wear tests of the unreinforced TiNbZr alloy and TiNbZr/TiB composites with an abrasive impact angle of 90° on the sample and an ejection speed of 30 m/s were carried out for 1 h. The erosive wear value was defined as the ratio between the lost volume of the material and the mass of abrasive particles expended during the test.

The biocompatibility of the composites and unreinforced alloy was analyzed by studying the local effect after implantation of the alloy samples under in vivo experiments. The local effect after implantation was assessed by implanting metal alloy disks into the subcutaneous tissue, as per ISO 10993-6-2021 [46] Part 6—"Local effect studies after implantation" recommendations. The samples exhibited disk shapes that were 5 mm in diameter and 1 mm thick. Implantation under the skin of an animal was carried out. Five samples from each group were used, as follows: group 1—Ti-6Al-4V alloy (control); group 2—unreinforced alloy; group 3—Alloy A; and group 4—Alloy B. The samples were implanted according to the scheme presented in Figure 1. The experiment duration was 9 weeks.

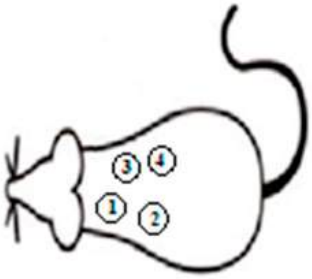

Figure 1. The sample implantation scheme. Each animal (out of five animals) was implanted with the following: the first subcutaneous pocket, with the Ti-6Al-4V alloy; the second subcutaneous pocket, with the unreinforced alloy; the third subcutaneous pocket, with Alloy A; and the fourth subcutaneous pocket, with Alloy B.

3. Results and Discussion

3.1. Initial Microstructure

The microstructure of the resulting as-cast composites consisted of the TiNbZr β matrix and multiple (Ti,Nb)B fibers (reported in detail in Ref. [25]) (Figures 2 and 3). The (Ti,Nb)B fibers had a needle-like shape with average diameters (cross-section size) of ~0.4 μm and ~2.0 μm for Alloys A and B, respectively. The homogeneity of distribution of (Ti,Nb)B fibers in the TiNbZr matrix increased with an increasing amount of reinforcements. The volume fractions of borides in the structures of the two states of the composites were found to be ~2.5% and ~12.4% for Alloys A and B, respectively. Coarse primary and fine eutectic borides were observed in Alloy B, suggesting a hypereutectoid composition, while only fine borides were formed in Alloy A [25]. The bimodal size distribution of borides is known to be attributed to the hypereutectic composition of the alloy, with large primary boride particles and small borides that are formed during the eutectic reaction (Figures 2b and 3) [23,47]. In contrast, large primary borides were not observed in Alloy A (Figure 2a), indicating its hypoeutectic composition.

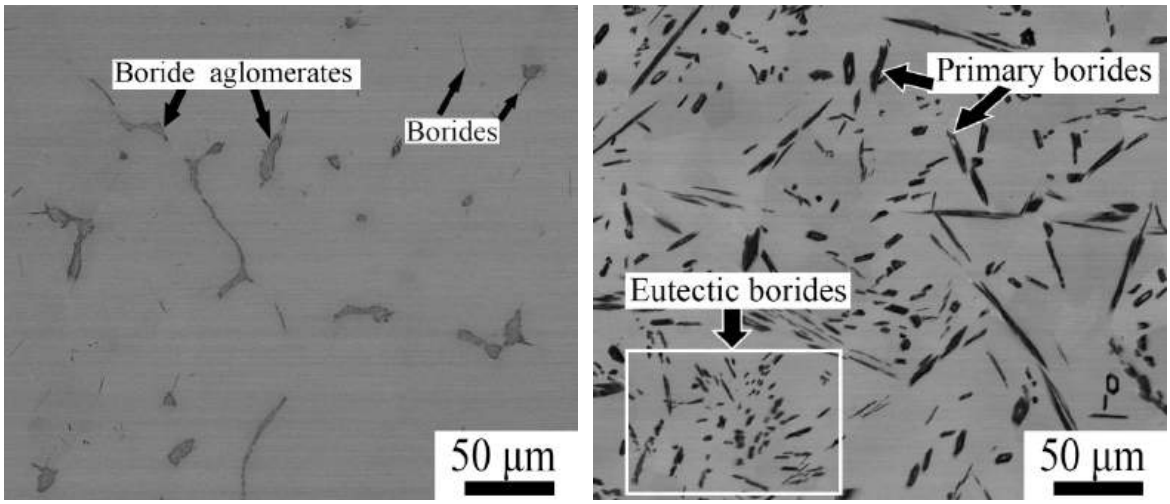

(**a**) (**b**)

Figure 2. Initial microstructure of the composites: (**a**) Alloy A; (**b**) Alloy B.

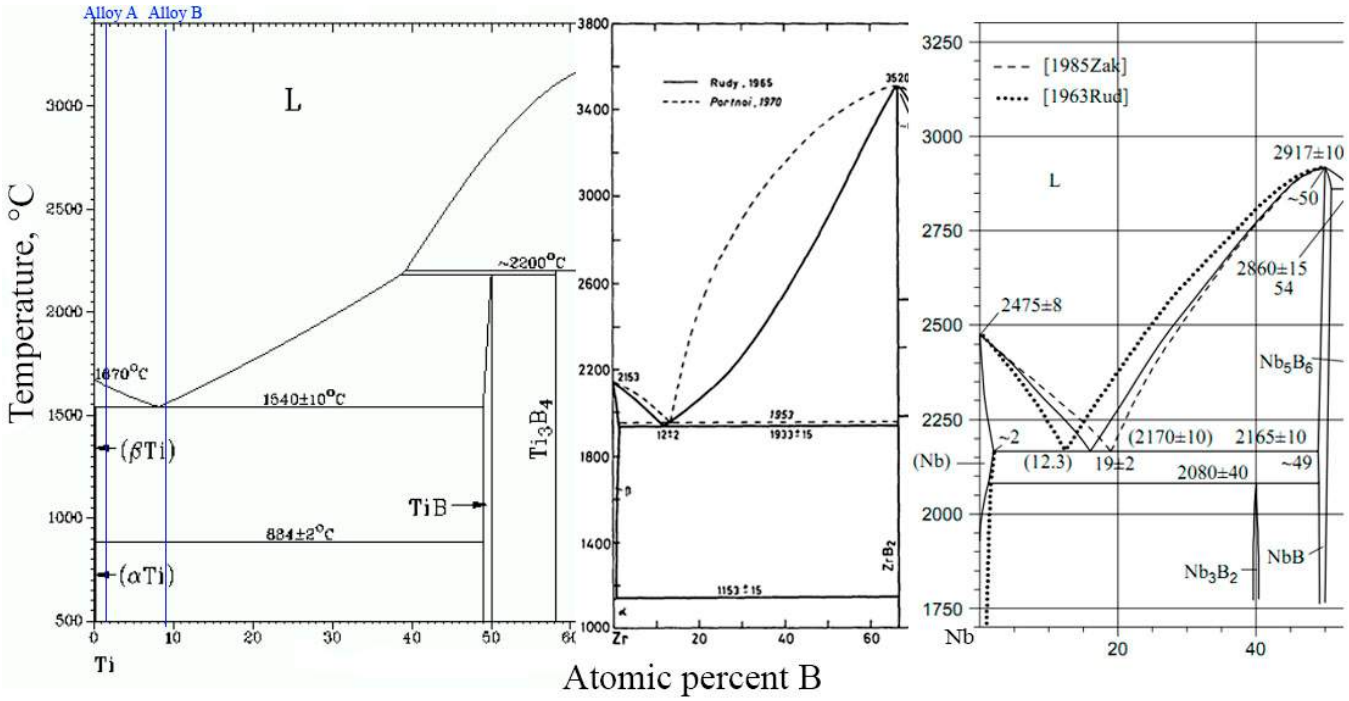

(**a**) (**b**) (**c**)

Figure 3. Phase diagrams of the (**a**) Ti-B; (**b**) Nb-B; and (**c**) Zr-B systems adapted from Refs. [48–50].

The X-ray diffraction analysis data reveal that the structure of the composites consisted of a (TiNbZr) bcc matrix and (Ti,Nb)B borides (Figure 4). The peaks corresponding to the bcc phase are identical to those previously observed for Ti–Nb–Zr alloys [5,7,11]. In turn, the peaks of the borides are similar to the peaks of TiB formed in alpha- or beta-titanium alloys [19,51,52]. It was found in our previous work [25] that (Ti,Nb)B fibers with a FeB-type orthorhombic crystal structure (oP8, Pnma) were formed during crystallization in the composite.

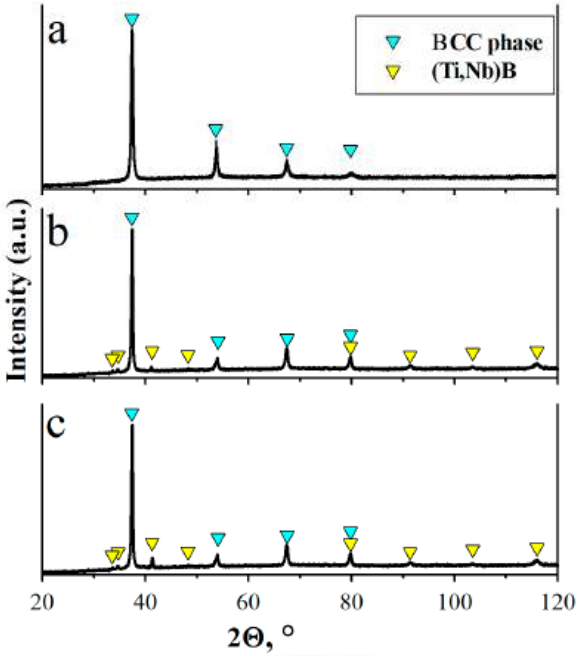

Figure 4. XRD patterns of (**a**) the unreinforced TiNbZr alloy; (**b**) Alloy A; and (**c**) Alloy B.

3.2. Mechanical Properties

After tensile testing at room temperature, the yield strength of Alloy A increased by ~100 MPa compared to that of the unreinforced TiNbZr alloy (Figure 5, Table 2), while its ductility dropped from 21 to 10%, which is not a critical value. As the TiB_2 content in Alloy B was increased to 4 wt. %, the yield strength rose to 750 MPa, while its ductility decreased to 0.5%. The Young's modulus values were 74.4, 75.4, and 113 GPa for the unreinforced alloy, Alloy A and Alloy B, respectively. The microhardness values were 190 ± 6, 238 ± 5 and 319 ± 8 HV for the unreinforced alloy, Alloy A and Alloy B, respectively (Table 2). Hence, these results show that the addition of boride reinforcing elements can significantly increase the strength of the medium-entropy TiNbZr alloy without critically reducing its Young's modulus.

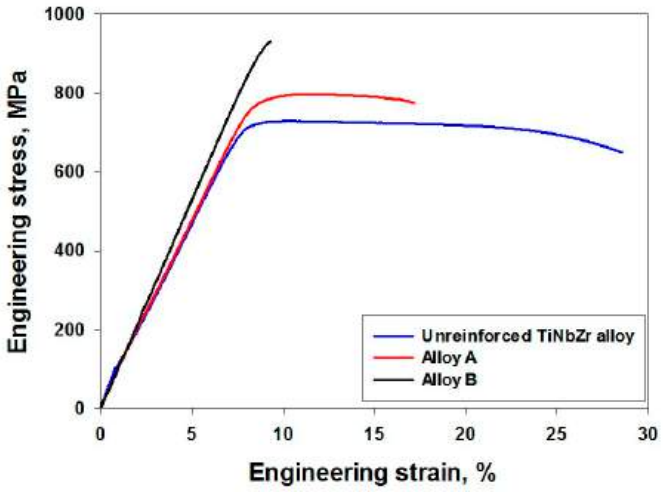

Figure 5. The flow curves recorded during tensile testing at 20 °C for the unreinforced TiNbZr alloy and TiNbZr–(Ti,Nb)B composite specimens.

Table 2. Mechanical properties of TiNbZr-(Ti,Nb)B composites with different TiB_2 weight contents compared to those of the unreinforced TiNbZr alloy.

State	Young's Modulus, GPa	Yield Strength, MPa	Ductility, %	Microhardness, HV
Unreinforced TiNbZr alloy	74.4 ± 0.05	650 ± 22	21 ± 2	190 ± 6
Alloy A	75.4 ± 0.05	750 ± 25	10 ± 1	238 ± 7
Alloy B	113 ± 0.05	900 ± 29	0.5 ± 0.1	319 ± 8

3.3. Corrosion Properties

The open-circuit potential (OCP) as a function of time suggests that all the samples were characterized by a rather high stability under the studied conditions. Moreover, for less than 20 min, variations in the OCP value did not exceed 15 mV (Figure 6a). The changes in the OCP of the unreinforced alloy within the period from 20 min to 90 min were 2 mV. The addition of 2.5% (Ti,Nb)B (Alloy A) increased the range of potential changes during the same time period to 8 mV. As the amount of (Ti,Nb)B in TiNbZr was further increased to 12.4% (Alloy B), oscillation rose to 15 mV. The presence of (Ti,Nb)B fibers, whose size was increasing with the percentage of TiB_2 in the charge mixture, possibly caused some changes in the nature of the redox reaction at the alloy–corrosion medium (solution) interface. The potentiodynamic polarization data for all the studied samples in 0.9% NaCl solution are shown in Figure 6b–e. One can see that all the studied states are characterized by the presence of a passivation region. For the unreinforced TiNbZr alloy, the passivation region is insignificant; the difference between the potential of the onset of passivation E_{op} and the potential of complete passivation E_{cp} is 110 mV. Passivation plays an important role in increasing the corrosion resistance of metals and alloys. A protective oxide film preventing dissolution is formed on the surface during this period. In the active state, the metal dissolves as the potential increases, and the formation of an oxide film reduces the dissolution rate. Thus, the abrupt rise in current density at stage 2 (line 2 in Figure 6b) can be associated with the dissolution process, but the current density decreased and the surface became less active once the passivation potential E_p had been reached. However, areas of repassivation with repeated surface activation can also emerge during the passivation stage. For the unreinforced alloy, an abrupt increase in current density was observed again when the potential value had reached 1730 mV, thereby suggesting the development of active corrosion dissolution processes. The addition of 2.5% (Ti,Nb)B decreased current density, although in general, the dependence of current density on potential remained similar (Figure 6b–e). Thus, the corrosion potentials were sufficiently similar for both the unreinforced alloy (E_{cor} = 1475 mV) and Alloy A (E_{cor} = 1488 mV); meanwhile, the corrosion current densities differed approximately 3.5-fold (Table 3), suggesting that the dissolution of the unreinforced state was more intense. As the (Ti,Nb)B content was increased to 12.4%, the corrosion current density rose compared to that of both the unreinforced alloy and Alloy A (Figure 6d,e, Table 1). Moreover, the first stage (line 1 in Figure 6d) of increasing the current density was more pronounced, while the second stage (line 2 in Figure 6d) and the passivation region were found to be more blurred. Furthermore, separate current density peaks (which can be associated with the onset of pitting) were observed in the potentiodynamic curve after 3600 mV. Hence, it can be inferred that the introduction of 12.4% (Ti,Nb)B into the alloy somewhat reduced the corrosion resistance of the alloy compared to both the unreinforced state and Alloy A. The comparison of the corrosion resistances of the resulting alloys with those of CP titanium and Ti-6Al-4V alloy, which are widely used in medicine, shows that the corrosion resistance of Alloy A remained similar to that of the CP alloy. Thus, for the CP alloy under similar test conditions, E_{OCP} = −290 mV and E_{cor} = 1581 mV, which are comparable with the values for Alloy A (Table 3) [53]. The corrosion potential of the

Ti-6Al-4V alloy slightly increased to 1858 mV, indicating that it is characterized by slightly better corrosion resistance compared to the CP alloy and Alloy A. However, all of these alloys show good corrosion resistance from the perspective of biomedical applications. The comparison of the corrosion resistance of the resulting alloys to that of commercially pure titanium, which is widely used in medicine, showed that the corrosion resistance of alloy A remained at the level of commercially pure titanium. The graph of changes in current density as a function of potential indicates that dissolution (i.e., an increase in current density) occurs at close potential values (Figure 6f). Thus, for commercially pure titanium, E_{cor} =1581 mV, which is comparable with the value for Alloy A, where E_{cor} = 1488 mV. Meanwhile, the corrosion current densities also differed insignificantly compared to those of other alloys presented in these studies, at 0.016 mA/cm^2 and 0.012 mA/cm^2 for Alloy A and commercially pure titanium, respectively (Figure 6f).

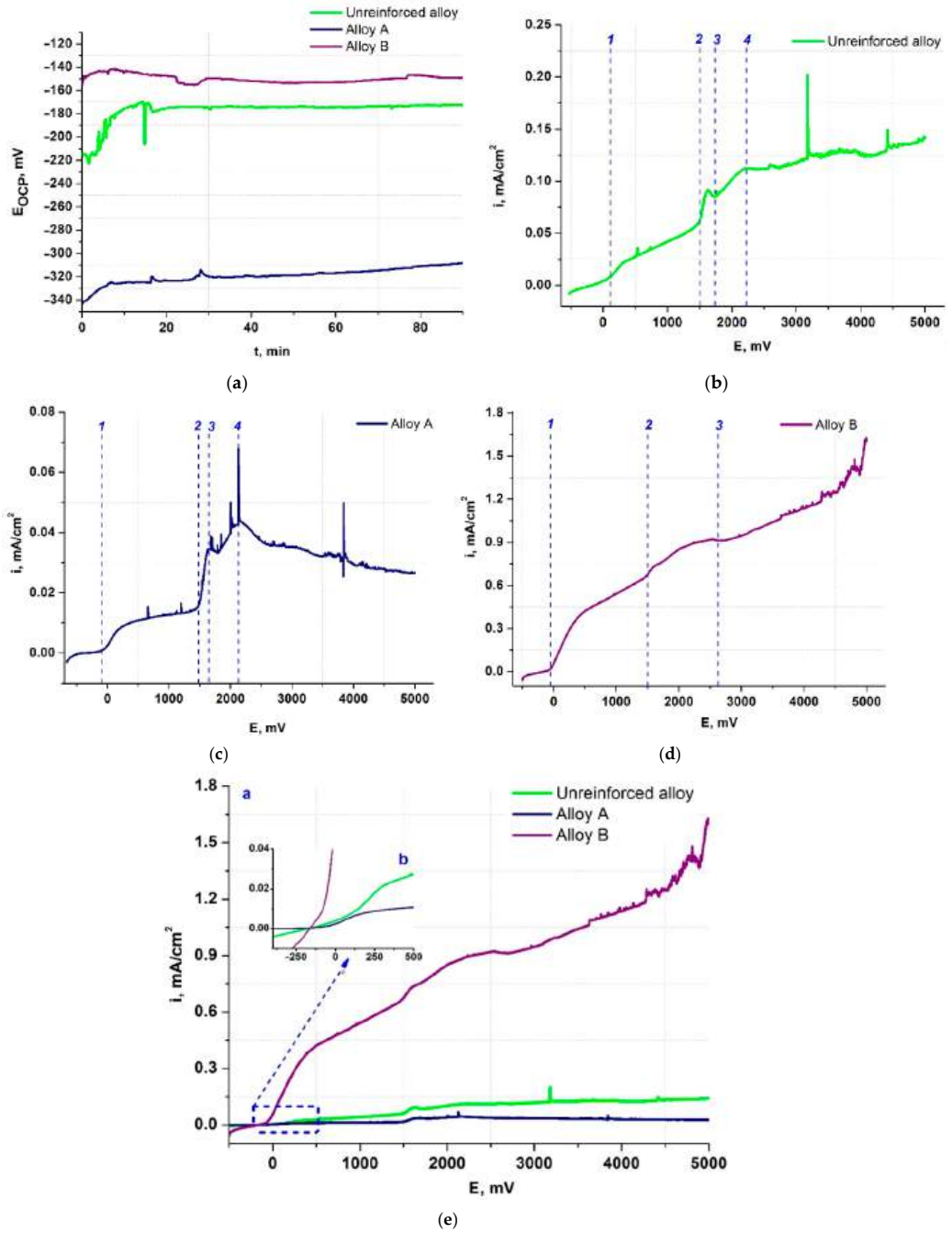

Figure 6. *Cont.*

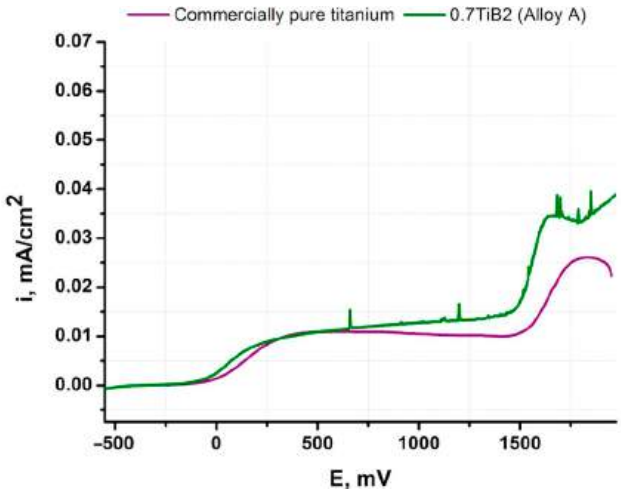

(**f**)

Figure 6. (**a**) The open circuit potential E_{OCP} for all alloys and (**b**–**e**) potentiodynamic polarization curves in 0.9%NaCl solution: (**a**,**b**) unreinforced alloy, (**c**) Alloy A, (**d**) Alloy B, (**e**) all alloys (a- general appearance, b- enlarged area) and (**f**) comparison of corrosion resistance values of the resulting alloys to that of commercially pure titanium.

Table 3. Summary table of indicators after corrosion resistance tests.

State	E_{OCP}, mV	E_{cor}, mV	$i_{cor} \times 10^{-2}$ mA/cm^2
Unreinforced alloy	−172	1475	5.8
Alloy A	−308	1488	1.6
Alloy B	−149	−72	1.2
CP titanium	290	1581	1.2

The analysis of the surface morphology of Alloy B after corrosion tests confirmed the formation of pits (Figure 7). Optical microscopy images suggest the passivation of the matrix surface (less contrasting areas in Figure 7a) in contrast to the (Ti,Nb)B particles (lighter areas); the latter is indicative of the formation of microgalvanic pairs and the dissolution of more electronegative elements. As a result, pitting is observed on the surface of the (Ti,Nb)B particles, and fine particles can dissolve almost completely, leading to the formation of pits reproducing the hexagonal form of borides (Figure 7b).

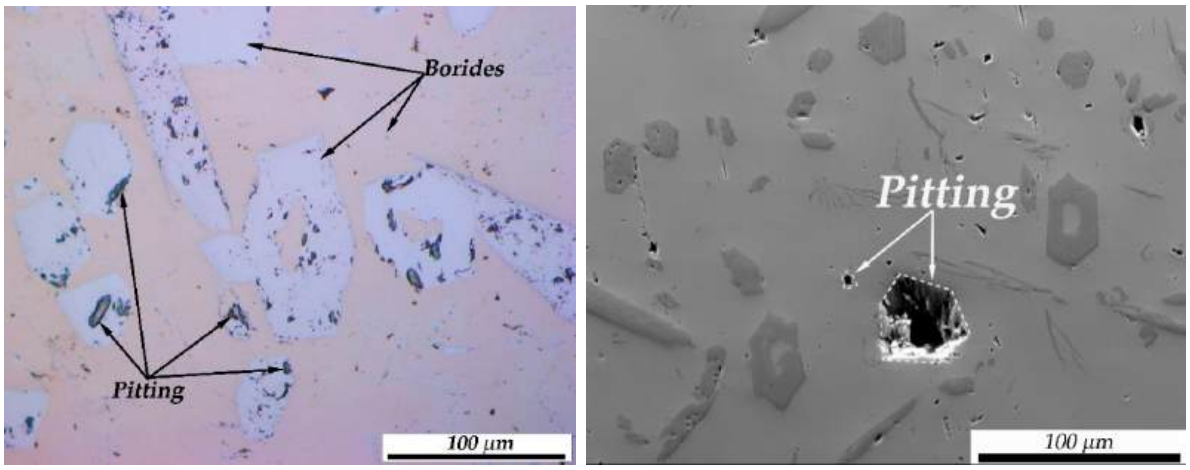

(**a**) (**b**)

Figure 7. (**a**) Optical microscopy and (**b**) SEM images of surface Alloy B after corrosion tests.

The much higher current density values seen during the corrosion test suggest that the dissolution of the unreinforced alloy sample in a corrosive environment is more intense compared to that of the composites. However, the obtained E_{OCP}, E_{cor} and I_{cor} values imply that the maximum content of borides associated with the best corrosion resistance was ~2.5%. Earlier, comparable results were published for the Ti–TiB composite [32–35]. Unfortunately, no comparative data on the corrosion resistance of TiNbZr–(Ti,Nb)B composites are available yet. It is worth noting that in Ref. [43], the addition of 0.5 wt. % boron to the Ti–13Zr–13Nb alloy deteriorated corrosion resistance. However, the rise in the (Ti,Nb)B content to 12.4% was accompanied by an increase in the corrosion current density and the development of pitting on the surface, thereby suggesting that the corrosion resistance of Alloy B was reduced compared to those of both the unreinforced alloy and Alloy A. The search for the optimal content of the reinforcing component with respect to the corrosion resistance of TiNbZr–(Ti,Nb)B composites deserves further attention.

3.4. Tribological Properties

An analysis of tribological characteristics has shown that the addition of (Ti,Nb)B reinforcements to the TiNbZr alloy somewhat reduced the friction coefficient (Figure 8). Thus, in the alloy with 2.5% (Ti,Nb)B (Alloy A), the friction coefficient decreased from 1.15 to 1.13 compared to that for the TiNbZr alloy. An increase in the volume fraction of (Ti,Nb)B to 12.4% (Alloy B) decreased the friction coefficient approximately twofold, from 1.15 to 0.58 (Table 4). It is worth noting that the behaviors of the friction coefficient as a function of friction path were quite similar for the unreinforced alloy and Alloy A. Thus, the running-in stage started with a reduction in the friction coefficient, followed by stabilization and an increase in the μ values after 60 m. Meanwhile, the friction coefficient curve for Alloy B can be divided into two stages (Figure 8). The first stage was characterized by quite a low friction coefficient (the average friction coefficient was 0.35 for the distance of 105 m). An abrupt increase in the friction coefficient occurred at the second stage, followed by some decrease. An analysis of the friction track surface revealed the presence of traces of abrasive wear, as well as the local presence of wear products in the friction contact area (Figure 9a). The abrasive wear mechanism involved the presence of grooves on the friction surface, formed as a result of hard abrasive activity (Figure 9b). Due to the presence of a harder (compared the matrix) abrasive, the plastic deformation was accompanied by the removal of material from the friction area and the formation of characteristic grooves. Similar grooves were observed on the friction track surface of Alloy B. The chemical analysis of the local areas, as well as the material transferred to the friction track surface, showed the presence of Fe due to the wearing of the steel counterbody, in addition to the elements constituting Alloy B (Ti, Nb, Zr). In the friction areas where only "grooves" were formed, no other elements in addition to elements comprising the matrix were revealed. Therefore, (Ti,Nb)B particles were most likely to act as abrasive particles. The abrupt increase in the friction coefficient after 105 m can therefore be associated with the ingress of large solid (Ti,Nb)B particles into the friction contact area. The described friction mechanism also confirms the higher wear factor for Alloy B specimens compared to those of both the unreinforced alloy and Alloy A (Table 4). Specifically, the wear factors for the unreinforced alloys and Alloy A were 4.14×10^{-4} mm^3/Hm and 4.39×10^{-4} mm^3/Hm, respectively, compared to 5.69×10^{-4} mm^3/Hm for Alloy B. The wear factor of the counterbody exhibited an opposite trend, i.e., the minimum wear factor of 1.91×10^{-5} mm^3/Hm corresponded to the alloys reinforced with (Ti,Nb)B, while the unreinforced alloy had the maximum wear factor. It is worth noting that the addition of even 2.5% (Ti,Nb)B into the alloy reduced the wear factor of the counterbody by a factor of ~1.5.

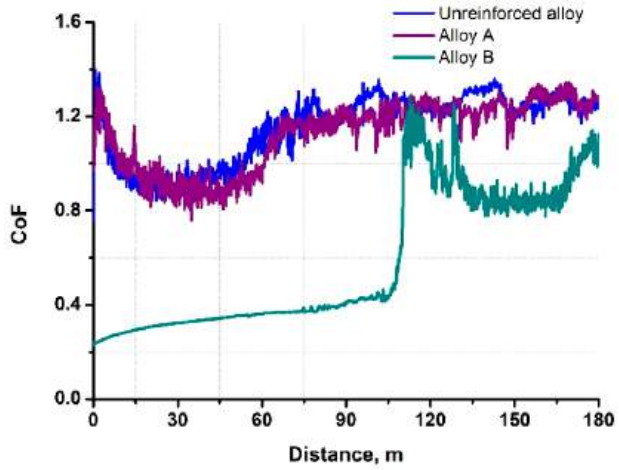

Figure 8. Friction coefficient CoF as a function of friction path under dry sliding friction conditions.

Table 4. Tribological characteristics of unreinforced alloy and composites.

State	Wear Factor of Samples, $\times 10^{-4}$ mm^3/Hm	Wear Factor of Ball, $\times 10^{-5}$ mm^3/Hm	Coefficient of Friction, μ
Unreinforced alloy	4.14	3.14	1.15
Alloy A	4.39	1.87	1.13
Alloy B	5.69	1.91	0.58

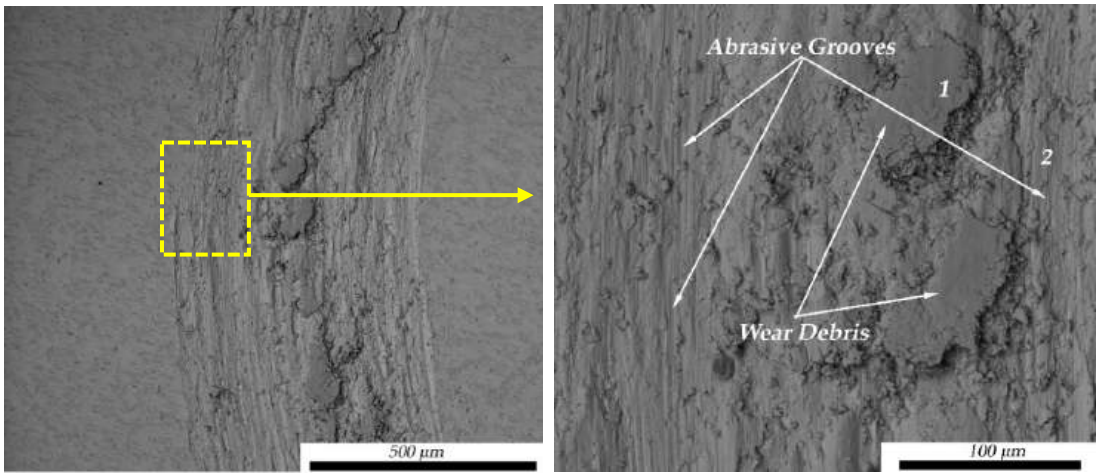

(**a**) (**b**)

Figure 9. The microstructure of friction tracks after a tribological test of Alloy B (**a**,**b**).

Appropriate tests were carried out to obtain a more complete picture of wear and assess the response of the material surface to erosive contact. The obtained erosion wear values show that the wear resistance of the composite samples was higher compared to that of the unreinforced equiatomic TiNbZr alloy (Table 5).

Table 5. Erosive wear rate of unreinforced alloy and composites.

State	Erosion Rate, mm^3/g
Unreinforced alloy	6.06×10^{-3}
Alloy A	5.71×10^{-3}
Alloy B	5.58×10^{-3}

The macroanalysis of the surface after erosion tests revealed no qualitative differences between the three states (Supplementary Material, Figure S1). Similarly, a microanalysis of the surface after erosion tests revealed no qualitative differences between the three states (Supplementary Material, Figure S2). One can see that the borides have no visible defects (Supplementary Material, Figure S2b,c).

A more detailed microstructural analysis of the cross-section of the surfaces after erosive wear revealed no differences in the reactions of the matrix structures of the unreinforced alloy and Alloy B (Figure 10a,b). However, microcracks were found in the borides located near the wear surface (Figure 10b, Supplementary Material, Figure S3). It is worth noting that the cracks propagated only within the (Ti,Nb)B fibers, without transitioning into the ductile TiNbZr matrix; no microcracks were observed at (along) the TiNbZr/(Ti,Nb)B interfaces (Figure 10b, Supplementary Material, Figure S3).

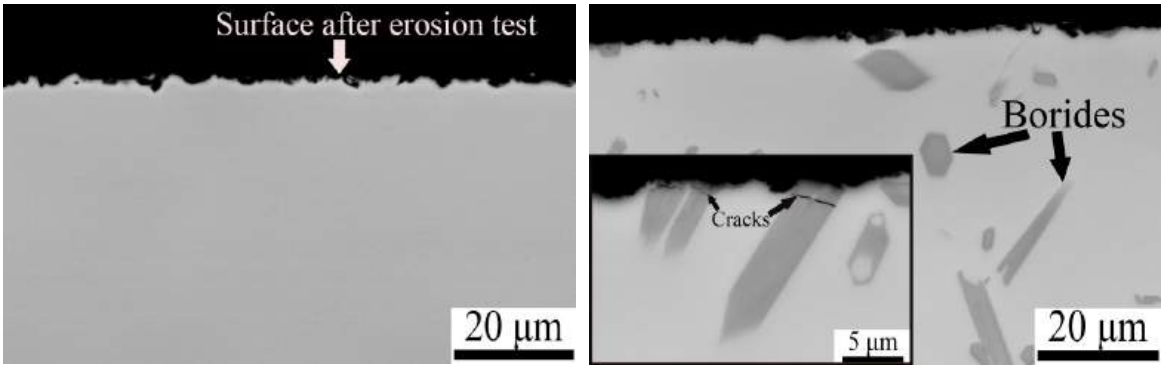

(**a**) (**b**)

Figure 10. Images of the surface after the wear of (**a**) unreinforced alloy and (**b**) Alloy B (cross-sections of the tested samples).

Therefore, two main conclusions can be drawn by analyzing the tribological properties of the unreinforced alloy and composites. On the one hand, the friction coefficient, which mainly indicates the wear resistance of the materials, showed better results for Alloys A and B compared to that of the unreinforced alloy. On the other hand, the wear factor values were higher for reinforced alloys, mainly for Alloy B. A similar phenomenon can be attributed [37,38] to the transition of the mechanism of adhesive wear of the surface in the case of the unreinforced alloy to strong abrasive wear in the case of Alloys A and B. Furthermore, for the composites (mainly for Alloy B), this mechanism is not activated immediately, but apparently after a certain degree of adhesion of solid (Ti,Nb)B fibers to the surface of the counterbody. In turn, the analysis of the wear factor of the counterbody exhibited an opposite trend, where the minimum wear factor corresponded to the composites, while the maximum wear factor corresponded to the unreinforced alloy. This result is not surprising, since in the case of composites, the adhering (Ti,Nb)B abrasive particles rather than the counterbody surface started to wear out. Some increase in wear resistance of the composites has also been confirmed by the results of the erosion tests, since the maximum erosive wear was associated with the unreinforced alloy.

3.5. Biocompatibility

During the observation of experimental animals, it was found that all the animals tolerated the surgical intervention well; after eight days, the formation of granulation tissue and scarring was noted at skin damage sites (Supplementary Material, Figure S4). Animals were actively feeding and moving around the cage.

An analysis of blood smears of animals after nine weeks of the experiment showed that the leukocyte count lay within a normal range, and no inflammatory response was detected (Figure 11).

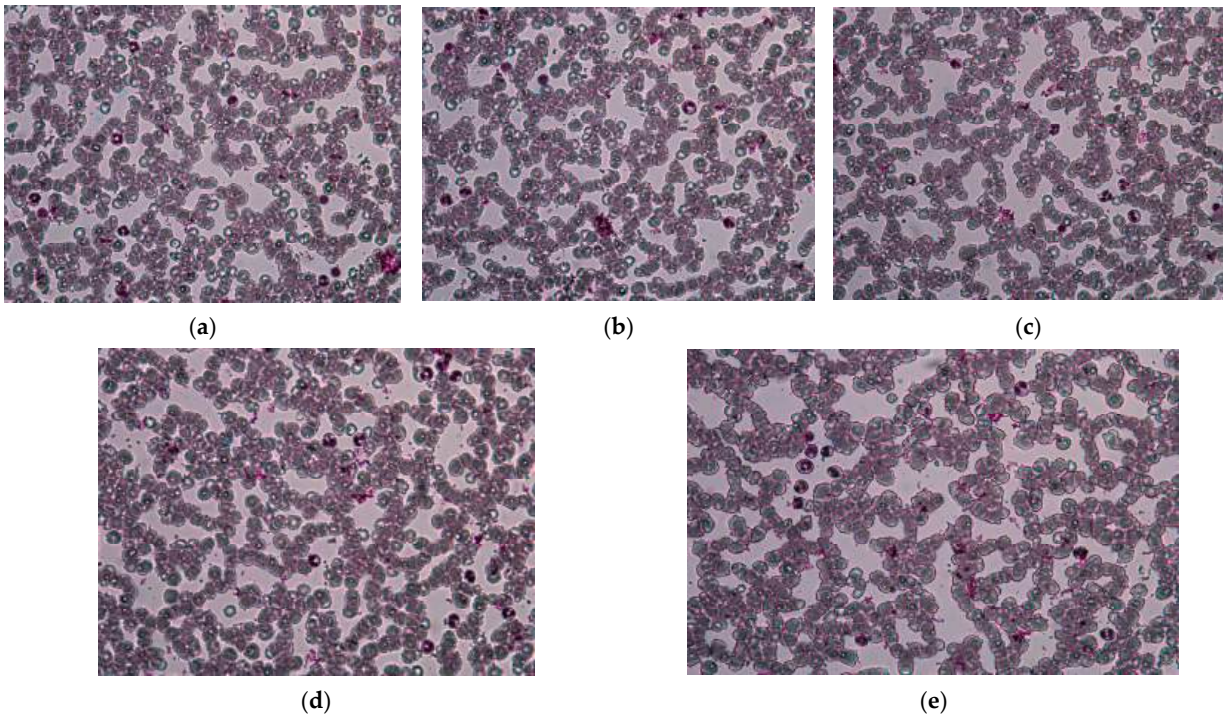

Figure 11. Fragments of a blood smear of the experimental animal: (**a**) No. 1, (**b**) No. 2, (**c**) No. 3, (**d**) No. 4, and (**e**) No. 5, nine weeks after the implantation; ×400 magnification.

After nine weeks of the experiment, all five experimental animals showed completely restored fur (Supplementary Material, Figure S5); no visible skin disorders or inflammatory responses were detected.

The implantation of the Ti-6Al-4V (control) alloy resulted in the formation of full-blooded capillaries with supporting fibroblastic structures both around the implants and in the capsule. No signs of inflammation, diapedetic hemorrhages or tissue necrosis around the samples were noted; the connective tissue capsule was moderately thick and translucent. Similarly, the implantation of the unreinforced alloy and Alloy A caused a rise in full-blooded capillaries with supporting fibroblastic structures both around the implants and in the capsule; the foci of diapedetic hemorrhages were noted in the inner layer of the capsules. There were no signs of inflammation or tissue necrosis around the samples; the connective tissue capsule was thin and transparent. Finally, the presence of full-blooded capillaries with supporting fibroblastic structures both around the implants and in the capsule was noted in the areas of contact with the implanted Alloy B. There were no signs of inflammation, diapedetic hemorrhages or tissue necrosis around the samples; the connective tissue capsule was moderately thick and translucent (Figure 12). The images in Figure 12 show full-blooded vessels located around and inside the formed connective tissue capsule.

Twenty histological specimens were prepared to gain an insight into tissue responses to the implantation of the studied alloy. In all the experimental groups, no pathological changes were found at the site of implant inoculation (Figure 13). In experimental groups No. 1 (control) and No. 4 (Alloy B, Figure 11), the fibrous band was moderately thick, while in groups No. 2 (unreinforced alloy) and No. 3 (Alloy A), the fibrous band was narrow. In all the experimental groups, no infiltrations with polymorphonuclear or mononuclear

cells, diapedetic hemorrhages, inflammation or tissue necrosis were detected. The skin morphology in the damaged area was completely restored.

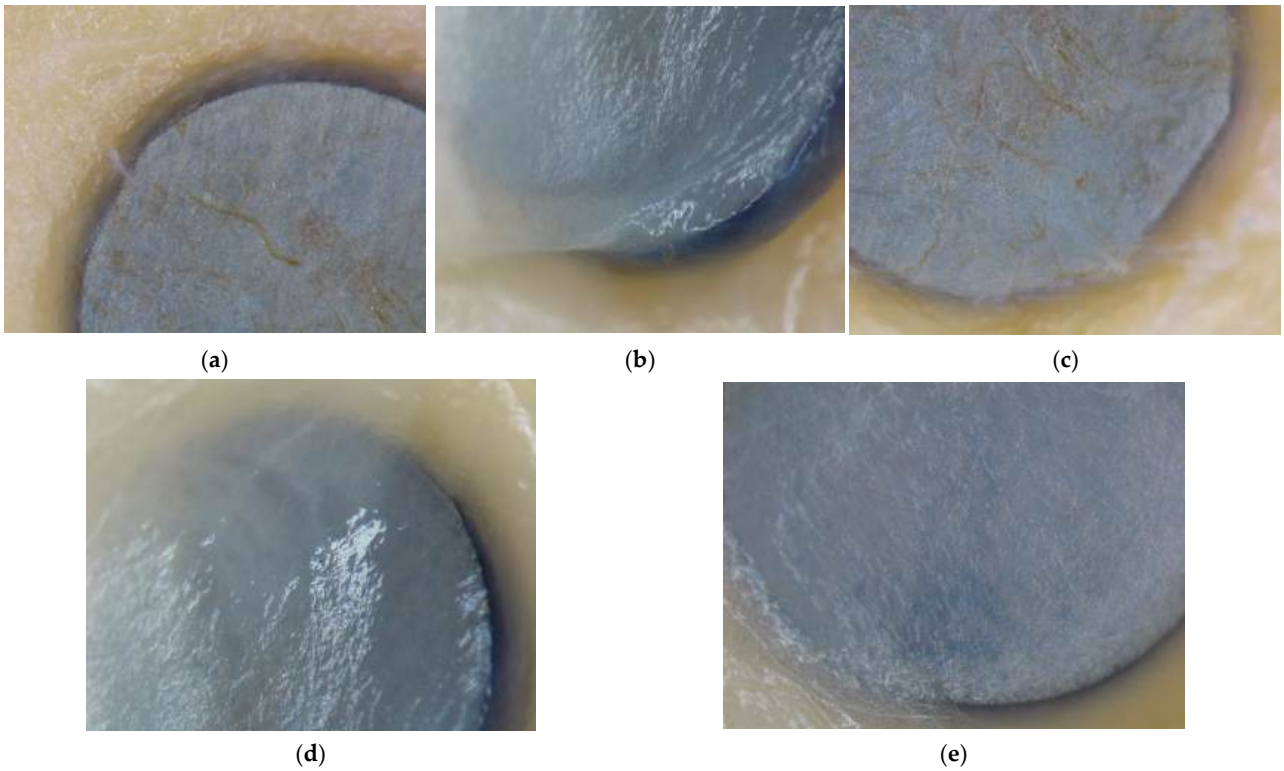

Figure 12. Fragments of encapsulated samples of Alloy B from the side of subcutaneous fat: (**a**) Animal No. 1; (**b**) animal No. 2; (**c**) animal No. 3; (**d**) animal No. 4; and (**e**) animal No. 5; ×200 magnification.

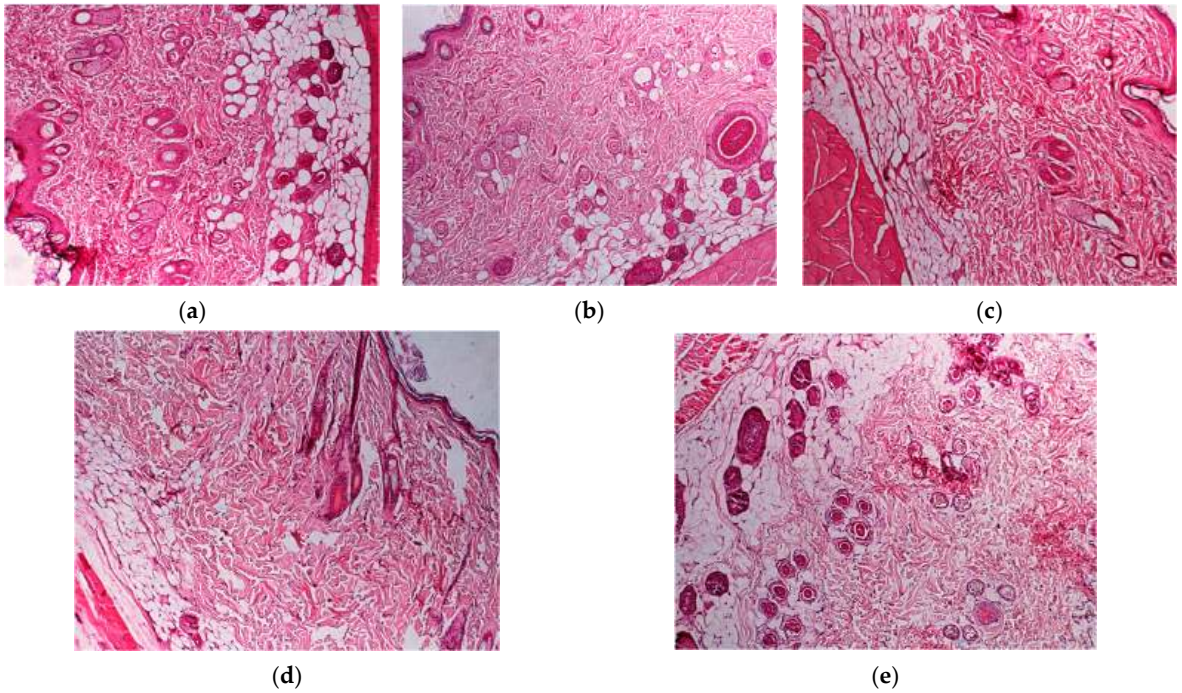

Figure 13. Fragment of a transverse section of a skin flap in direct contact with the connective tissue capsule of Alloy B: (**a**) Animal No. 1; (**b**) animal No. 2; (**c**) animal No. 3; (**d**) animal No. 4; and (**e**) animal No. 5. Hematoxylin and eosin staining; ×100 magnification.

In vivo experiments revealed no irritating effect for each studied group of material, i.e., No. 1 (Ti-6Al-4V alloy, control), No. 2 (unreinforced alloy), No. 3 (Alloy A), and No. 4 (Alloy B). Diapedetic hemorrhages were detected only in the loose fibrous connective tissue capsule (the inner layer) that was in direct contact with the surface of the unreinforced alloy and Alloy A. This result can, in fact, be associated with the weak fixation of the implants by the connective tissue capsule, which was traumatizing for the surrounding tissues when displaced. The biological responses of the tissues in the inoculation zones of metal alloys (implants of the experimental groups (Nos. 2, 3, and 4)) did not differ from those seen for group No. 1 (control), thereby suggesting the good biocompatibility of the composites. Similar results showing good biocompatibility were obtained earlier for the Ti–TiB composites [28,35,54].

The results obtained in this extensive experimental study allow us to confidently state that TiNbZr-(Ti,Nb)B composites can be considered promising biocompatible and bioapplicable materials. This paper shows the generally favorable effect of alloying equiatomic TiNbZr alloy with borides on corrosion resistance, wear resistance, and biocompatibility. We have successfully demonstrated that alloying an equiatomic TiNbZr matrix with (Ti,Nb)B fibers not only enhances the combination of mechanical properties of composites, without critically increasing the Young's modulus [25–27], but it also does not worsen, and in some cases even improves, the corrosion resistance, wear resistance and biocompatibility of the resulting TiNbZr–(Ti,Nb)B composite. It is worth noting that equiatomic TiNbZr alloys have already proved themselves to be corrosion-resistant and biocompatible materials. It was shown in Refs. [5,11,55] that equiatomic TiNbZr alloys have excellent corrosion resistance and biocompatibility, even surpassing those of the well-known alloy. However, the few studies on the effects of doping with boron have shown its negative effect on the corrosion resistance of the Ti–13Zr–13Nb alloy [43]. In this work, we did not observe such effects. The wear resistance findings also deserve attention, showing that the addition of titanium diboride to the TiNbZr alloy reduces the friction coefficient. In Ref. [25], we had already conducted experiments to determine the in vitro cytotoxicity of TiNbZr–(Ti,Nb)B composites. More in-depth experiments of in vivo biocompatibility have been conducted in this study. It is worth noting that the TiNbZr–(Ti,Nb)B composites have proved themselves to be excellent biocompatible materials.

4. Conclusions

TiNbZr–TiB composites were obtained by vacuum arc melting using Ti, Nb, and Zr in the equiatomic proportion with different weight fractions of TiB_2 powder in the charge mixture. The amounts of TiB_2 were 0.7 (Alloy A) and 4.0 (Alloy B) wt. %; the unreinforced TiNbZr alloy was also fabricated using the same method, without adding TiB_2. The following conclusions could be drawn based on the obtained results:

1. The microstructure of the composites consisted of the TiNbZr β matrix and (Ti,Nb)B fibers. The (Ti,Nb)B fibers had a needle-like shape with the average diameter of ~0.4 and ~2.0 μm for Alloys A and B, respectively. The volume fractions of the borides in the structures of the two states of the composites were found to be ~2.5 and ~12.4% for Alloys A and B, respectively;
2. The addition of 12.4% of (Ti,Nb)B was shown to deteriorate the corrosion resistance of Alloy B compared to that of the unreinforced TiNbZr alloy and Alloy A. Alloy A and the unreinforced alloy showed similar corrosion resistance values;
3. Tribological tests showed that the introduction of boride particles to the TiNbZr alloy reduced the friction coefficient from 1.15 for the unreinforced alloy to 1.13 for Alloy A (2.5% of (Ti,Nb)B), and reduced it twofold, from 1.15 to 0.58, for Alloy B, with 12.4% of (Ti,Nb)B;

4. The full biocompatibility of the TiNbZr–(Ti,Nb)B composites was established during in vivo experiments. No significant differences were found between the Ti-6Al-4V alloy, the unreinforced TiNbZr alloy and TiNbZr–(Ti,Nb)B composites containing 2.5% and 12.4% borides.

Supplementary Materials: The following supporting information can be downloaded at: https://www.mdpi.com/article/10.3390/met15030240/s1, Figure S1: Macro photographs of the surface of unreinforced alloy (a), Alloy A (b) and Alloy B (c) after erosive wear tests; Figure S2: Images of the surface relief of unreinforced alloy (a), Alloy A (b) and Alloy B (c) after erosive wear tests; Figure S3: Images of the surface after wear of Alloy B (cross section of the tested samples); Figure S4: The surface of the back of rat No. 1 on the 8th day of the experiment; Figure S5: Complete restoration of fur of experimental animals (after 9 weeks of experiment).

Author Contributions: Conceptualization, V.S. and M.O.; methodology, M.O., E.P., M.G., S.N. and M.Y.; validation, V.S. and M.O.; formal analysis, M.O., E.P., M.G., F.Y., D.T., S.N. and M.Y.; investigation, M.G., S.N., E.P., F.Y. and M.Y.; resources, V.S., S.N., D.T. and M.O.; data curation, V.S., S.N., D.T. and M.O.; writing—original draft preparation, V.S.; writing—review and editing, S.N., M.G. and M.O.; visualization, V.S., F.Y., D.T. and M.G.; supervision, V.S. and M.O.; project administration, M.O.; funding acquisition, M.O. All authors have read and agreed to the published version of the manuscript.

Funding: This research was funded by the Russian Science Foundation, Grant Number No. 22-19-00476.

Data Availability Statement: The original contributions presented in this study are included in the article/supplementary material. Further inquiries can be directed to the corresponding authors.

Acknowledgments: The authors gratefully acknowledge the financial support from the Russian Science Foundation (Grant Number No. 22-19-00476). A part of this research (SEM characterization) was partially funded by the Ministry of Science and Higher Education of the Russian Federation as part of the World-Class Research Center program: Advanced Digital Technologies (Contract No. 075-15-2022-312 dated 20 April 2022). The authors are grateful to the personnel of the Joint Research Center, Belgorod State National Research University for their assistance with the instrumental analysis.

Conflicts of Interest: The authors declare no conflicts of interest.

References

1. Zhang, L.C.; Chen, L.Y. A Review on Biomedical Titanium Alloys: Recent Progress and Prospect. *Adv. Eng. Mater.* **2019**, *21*, 1801215. [CrossRef]
2. Okazaki, Y. A new Ti-15Zr-4Nb-4Ta alloy for medical applications. *Curr. Opin. Solid State Mater. Sci.* **2001**, *5*, 45–53. [CrossRef]
3. Flaten, T.P. Aluminium as a risk factor in Alzheimer's disease, with emphasis on drinking water. *Brain Res. Bull.* **2001**, *55*, 187–196. [CrossRef]
4. Lima, P.D.; Vasconcellos, M.C.; Montenegro, R.C.; Bahia, M.O.; Costa, E.T.; Antunes, L.M. Genotoxic effects of aluminum, iron and manganese in human cells and experimental systems: A review of the literature. *Hum. Exp. Toxicol.* **2011**, *30*, 1435–1444. [CrossRef] [PubMed]
5. Ozan, S.; Lin, J.; Li, Y.; Ipek, R.; Wen, C. Development of Ti–Nb–Zr alloys with high elastic admissible strain for temporary orthopedic devices. *Acta Biomater.* **2015**, *20*, 176–187. [CrossRef] [PubMed]
6. Laheurte, P.; Prima, F.; Eberhardt, A.; Gloriant, T.; Wary, M.; Patoor, E. Mechanical properties of low modulus β titanium alloys designed from the electronic approach. *J. Mech. Behav. Biomed. Mater.* **2010**, *3*, 565–573. [CrossRef] [PubMed]
7. Senkov, O.N.; Rao, S.; Chaput, K.J.; Woodward, C. Compositional effect on microstructure and properties of NbTiZr-based complex concentrated alloys. *Acta Mater.* **2018**, *151*, 201–215. [CrossRef]
8. Geetha, M.; Singh, A.K.; Asokamani, R.; Gogia, A.K. Ti based biomaterials, the ultimate choice for orthopaedic implants—A review. *Prog. Mater. Sci.* **2009**, *54*, 397–425. [CrossRef]
9. Black, J. *Biological Performance of Materials, Fundamentals of Biocompatibility*; CRC Taylor & Francis: Boca Raton, FL, USA, 2006.
10. Huiskes, R.; Weinans, H.; Vanrietbergen, B. The relationship between stress shielding and bone-resorption around total hip stems and the effects of flexible materials. *Clin. Orthop. Relat. Res.* **1992**, *274*, 124–134. [CrossRef]

11. Meng, Q.; Guo, S.; Liu, Q.; Hu, L.; Zhao, X. A β-type TiNbZr alloy with low modulus and high strength for biomedical applications. *Prog. Nat. Sci. Mater. Int.* **2014**, *24*, 157–162. [CrossRef]
12. Rho, J.Y.; Tsui, T.Y.; Pharr, G.M. Elastic properties of human cortical and trabecular lamellar bone measured by nanoindentation. *Biomaterials* **1997**, *18*, 1325–1330. [CrossRef] [PubMed]
13. Hanawa, T.; Hiromoto, S.; Asami, K.; Okuno, O.; Asaoka, K. Surface oxide films on titanium alloys regenerated in Hanks' solution. *Mater. Trans.* **2002**, *43*, 3000–3004. [CrossRef]
14. Mishchenko, O.; Ovchynnykov, O.; Kapustian, O.; Pogorielov, M. New Zr-Ti-Nb Alloy for Medical Application: Development, Chemical and Mechanical Properties, and Biocompatibility. *Materials* **2020**, *13*, 1306. [CrossRef]
15. Aguilar Maya, A.E.; Grana, D.R.; Hazarabedian, A.; Kokubu, G.A.; Luppo, M.I.; Vigna, G. Zr–Ti–Nb porous alloys for biomedical application. *Mater. Sci. Eng. C* **2012**, *32*, 321–329. [CrossRef]
16. Hayat, M.D.; Singh, H.; He, Z.; Cao, P. Titanium metal matrix composites: An overview. *Compos. Part A Appl. Sci. Manuf.* **2019**, *121*, 418–438. [CrossRef]
17. Huang, L.; An, Q.; Geng, L.; Wang, S.; Jiang, S.; Cui, X.; Zhang, R.; Sun, F.; Jiao, Y.; Chen, X.; et al. Multiscale Architecture and Superior High-Temperature Performance of Discontinuously Reinforced Titanium Matrix Composites. *Adv. Mater.* **2021**, *33*, 2000688. [CrossRef] [PubMed]
18. Shetty, R.; Hegde, A.; Shetty SV, U.K.; Nayak, R.; Naik, N.; Nayak, M. Processing and Mechanical Characterisation of Titanium Metal Matrix Composites: A Literature Review. *J. Compos. Sci.* **2022**, *6*, 388. [CrossRef]
19. Ozerov, M.; Klimova, M.; Sokolovsky, V.; Stepanov, N.; Popov, A.; Boldin, M.; Zherebtsov, S. Evolution of microstructure and mechanical properties of Ti/TiB metal-matrix composite during isothermal multiaxial forging. *J. Alloys Compd.* **2019**, *770*, 840–848. [CrossRef]
20. Ravi Chandran, K.S.; Panda, K.B.; Sahay, S.S. TiBw-reinforced Ti composites: Processing, properties, application, prospects, and research needs. *JOM* **2004**, *56*, 42–48. [CrossRef]
21. Morsi, K. Review: Titanium–titanium boride composites. *J. Mater. Sci.* **2019**, *54*, 6753–6771. [CrossRef]
22. Samuel, S.; Nag, S.; Scharf, T.W.; Banerjee, R. Wear resistance of laser-deposited boride reinforced Ti-Nb-Zr-Ta alloy composites for orthopedic implants. *Mater. Sci. Eng. C* **2008**, *28*, 414–420. [CrossRef]
23. Nag, S.; Samuel, S.; Puthucode, A.; Banerjee, R. Characterization of novel borides in Ti-Nb-Zr-Ta + 2B metal-matrix composites. *Mater. Charact.* **2009**, *60*, 106–113. [CrossRef]
24. Majumdar, P.; Singh, S.B.; Dhara, S.; Chakraborty, M. Influence of in situ TiB reinforcements and role of heat treatment on mechanical properties and biocompatibility of β Ti-alloys. *J. Mech. Behav. Biomed. Mater.* **2012**, *10*, 1–12. [CrossRef] [PubMed]
25. Ozerov, M.; Sokolovsky, V.; Nadezhdin, S.; Zubareva, E.; Zherebtsova, N.; Stepanov, N.; Huang, L.; Zherebtsov, S. Microstructure and mechanical properties of medium-entropy TiNbZr alloy-based composites, reinforced with boride particles. *J. Alloys Compd.* **2023**, *938*, 168512. [CrossRef]
26. Ozerov, M.; Sokolovsky, V.; Stepanov, N.; Zherebtsov, S. Microstructure and tensile properties of TiNbZr alloy-based metal-matrix composites, reinforced with borides. *AIP Conf. Proc.* **2023**, *2899*, 020109.
27. Ozerov, M.; Sokolovsky, V.; Yurchenko, N.; Astakhov, I.; Povolyaeva, E.; Plekhov, O.; Tagirov, D.; Stepanov, N.; Zherebtsov, S. Effect of Cold Rolling on Microstructure and Mechanical Properties of a Cast TiNbZr-Based Composite Reinforced with Borides. *Metals* **2024**, *14*, 104. [CrossRef]
28. Makau, F.M.; Morsi, K.; Gude, N.; Alvarez, R.; Sussman, M.; May-Newman, K. Viability of Titanium-Titanium Boride Composite as a Biomaterial. *ISRN Biomater.* **2013**, *1*, 970535. [CrossRef]
29. Kabu, M.; Akosman, M.S. Biological Effects of Boron. *Rev. Environ. Contam. Toxicol.* **2013**, *225*, 57–75. [PubMed]
30. Nielsen, F.H. Update on human health effects of boron. *J. Trace Elem. Med. Biol.* **2014**, *28*, 383–387. [CrossRef] [PubMed]
31. Otte, J.A.; Zou, J.; Patel, R.; Lu, M.; Dargusch, M.S. TiB Nanowhisker Reinforced Titanium Matrix Composite with Improved Hardness for Biomedical Applications. *Nanomaterials* **2020**, *10*, 2480. [CrossRef]
32. Aljafery, A.M.A.; Fatalla, A.A.; Haider, J. Cytotoxicity, Corrosion Resistance, and Wettability of Titanium and Ti-TiB_2 Composite Fabricated by Powder Metallurgy for Dental Implants. *Metals* **2024**, *14*, 538. [CrossRef]
33. Chen, Y.; Zhang, J.; Dai, N.; Qin, P.; Attar, H.; Zhang, L.-C. Corrosion Behaviour of Selective Laser Melted Ti-TiB Biocomposite in Simulated Body Fluid. *Electrochim. Acta* **2017**, *232*, 89–97. [CrossRef]
34. Ozerov, M.; Gazizova, M.; Zherebtsova, N.; Stepanov, N.; Zherebtsov, S. Corrosion properties of a Ti-15Mo/TiB composite produced by spark plasma sintering. *AIP Conf. Proc.* **2019**, *2167*, 020260.
35. Bahl, S.; Raj, S.; Vanamali, S.; Suwas, S.; Chatterjee, K. Effect of boron addition and processing of Ti–6Al–4V on corrosion behaviour and biocompatibility. *Mater. Technol.* **2014**, *29*, 64–68. [CrossRef]
36. Attar, H.; Ehtemam-Haghighi, S.; Kent, D.; Okulov, I.V.; Wendrock, H.; Bönisch, M.; Volegov, A.S.; Calin, M.; Eckert, J.; Dargusch, M.S. Nanoindentation and wear properties of Ti and Ti-TiB composite materials produced by selective laser melting. *Mater. Sci. Eng. A* **2017**, *688*, 20–26. [CrossRef]

37. Ozerov, M.; Stepanov, N.; Zherebtsov, S. Wear resistance of Ti/TiB composites produced by spark plasma sintering. *AIP Conf. Proc.* **2017**, *1909*, 020164.
38. Yazdi, R.; Kashani-Bozorg, S.F. Microstructure and wear of in-situ Ti/(TiN + TiB) hybrid composite layers produced using liquid phase process. *Mater. Chem. Phys.* **2015**, *152*, 147–157. [CrossRef]
39. Sivakumar, B.; Singh, R.; Pathak, L.C. Corrosion behavior of titanium boride composite coating fabricated on commercially pure titanium in Ringer's solution for bioimplant applications. *Mater. Sci. Eng. C* **2015**, *48*, 243–255. [CrossRef] [PubMed]
40. Sivakumar, B.; Pathak, L.C.; Singh, R. Response of boride coating on the Ti-6Al-4V alloy to corrosion and fretting corrosion behavior in Ringer's solution for bio-implant application. *Appl. Surf. Sci.* **2018**, *433*, 1158–1174.
41. Majumdar, P.; Singh, S.B.; Chakraborty, M. Wear properties of Ti–13Zr–13Nb (wt.%) near β titanium alloy containing 0.5 wt.% boron in dry condition, Hank's solution and bovine serum. *Mater. Sci. Eng. C* **2010**, *30*, 1065–1075. [CrossRef]
42. Majumdar, P.; Singh, S.B.; Dhara, S.; Chakraborty, M. Influence of boron addition to Ti–13Zr–13Nb alloy on MG63 osteoblast cell viability and protein adsorption. *Mater. Sci. Eng. C* **2015**, *46*, 62–68. [CrossRef]
43. Majumdar, P.; Singh, S.B.; Chatterjee, U.K.; Chakraborty, M. Corrosion behaviour of heat treated boron free and boron containing Ti–13Zr–13Nb (wt%) alloy in simulated body fluid. *J. Mater. Sci. Mater. Med.* **2011**, *22*, 797–807. [CrossRef]
44. *ASTMG99-959*; Standard Test Method for Wear Testing with a Pin-on-Disk Apparatus. ASTM International: West Conshohocken, PA, USA, 2000.
45. *DIN50324*; Tribology; Testing of Friction and Wear Model Test for Sliding Friction of Solids (Ball-on-Disc System). DIN: Berlin, Germany, 1992.
46. *ISO 10993-6-2021*; Medical Devices. Biological Evaluation of Medical Devices. Part 6. Tests for Local Effects after Implantation. ISO: Moscow, Russia, 2021.
47. An, Q.; Huang, L.; Qian, Q.; Jiang, Y.; Wang, S.; Zhang, R.; Geng, L.; Wang, L. Insights into in-situ TiB/dual-phase Ti alloy interface and its high load-bearing capacity. *J. Mater. Sci. Technol.* **2022**, *119*, 156–166. [CrossRef]
48. Murray, J.L.; Liao, P.K.; Spear, K.E. The B−Ti (Boron-Titanium) system. *Bull. Alloy Phase Diagr.* **1986**, *7*, 550–555. [CrossRef]
49. Rogl, P.; Potter, P.E. A critical review and thermodynamic calculation of the binary system: Zirconium-boron. *Calphad* **1988**, *12*, 191–204. [CrossRef]
50. Rogl, P.; Korniyenko, K.; Velikanova, T. Boron—Carbon—Niobium. *Calphad* **2009**, *1*, 1–25. [CrossRef]
51. Ozerov, M.; Klimova, M.; Kolesnikov, A.; Stepanov, N.; Zherebtsov, S. Deformation behavior and microstructure evolution of a Ti/TiB metal-matrix composite during high-temperature compression tests. *Mater. Des.* **2016**, *112*, 17–26. [CrossRef]
52. Zherebtsov, S.; Ozerov, M.; Povolyaeva, E.; Sokolovsky, V.; Stepanov, N.; Moskovskikh, D.; Salishchev, G. Effect of hot rolling on the microstructure and mechanical properties of a Ti-15Mo/TiB metal-matrix composite. *Metals* **2020**, *10*, 40. [CrossRef]
53. Gazizova, M.Y.; Ivanov, M.B.; Vershinina, T.N. Investigation of Corrosion Behavior of Bioactive Coverings on Commercially Pure Titanium and its Alloys. *J. Nano-Electron. Phys.* **2015**, *7*, 04081.
54. Kaczmarek, M.; Jurczyk, M.U.; Miklaszewski, A.; Paszel-Jaworska, A.; Romaniuk, A.; Lipińska, N.; Żurawski, J.; Urbaniak, P.; Jurczyk, K. In vitro biocompatibility of titanium after plasma surface alloying with boron. *Mater. Sci. Eng. C* **2016**, *69*, 1240–1247. [CrossRef] [PubMed]
55. Hu, M.; Wang, L.; Li, G.; Huang, Q.; Liu, Y.; He, J.; Wu, H.; Song, M. Investigations on microstructure and properties of Ti-Nb-Zr medium-entropy alloys for metallic biomaterials. *Intermetallics* **2022**, *145*, 107568. [CrossRef]

Disclaimer/Publisher's Note: The statements, opinions and data contained in all publications are solely those of the individual author(s) and contributor(s) and not of MDPI and/or the editor(s). MDPI and/or the editor(s) disclaim responsibility for any injury to people or property resulting from any ideas, methods, instructions or products referred to in the content.